GEOPHYSICS, VOL. 81, NO. 3 (MAY-JUNE 2016); P. 1–12, 12 FIGS.
10.1190/GEO2015-0417.1

Shear-wave velocity structure of the shallow sediments in the Bohai Sea from an ocean-bottom-seismometer survey

Yuan Wang[1], Zhiwei Li[2], Qingyu You[3], Tianyao Hao[3], Jian Xing[1], Lihua Liu[1], Chunlei Zhao[3], Xuelei Li[1], Litian Hu[1], and Paul Somerville[4]

ABSTRACT

To investigate the seismic velocity structure of the shallow sediments in the Bohai Sea of China, we conducted an shear-wave velocity inversion of the surface-wave dispersion data from a survey of 12 ocean-bottom seismometers (OBSs) and 377 shots of a 9000 in^3 air gun. With OBS station spacing of approximately 5 km and air-gun shot spacing of approximately 190 m, high-quality Scholte-wave data were recorded by the OBSs within 0.4–5 km offset. We retrieved the Scholte-wave phase-velocity dispersion for the fundamental mode and first overtone in the frequency band of 0.9–3.0 Hz with the phase-shift method and inverted for the shear-wave velocity structure of the shallow sediments with a damped iterative least-squares algorithm. Pseudo-2D shear-wave velocity profiles with a depth of approximately 400 m revealed coherent features of relatively weak lateral velocity variation. We also estimated the uncertainty in shear-wave velocity structure based on the pseudo-2D profiles from six trial inversions with different initial models, which suggested a velocity uncertainty less than 30 m/s for most parts of the 2D profiles. The layered structure with little lateral variation may be attributable to the continuous sedimentary environment in the Cenozoic sedimentary basin of the Bohai Bay basin. The shear-wave velocity of $200 - 300$ m/s in the top 100 m of the Bohai seafloor may provide important information for offshore site response studies in earthquake engineering. Furthermore, the very low shear-wave velocity structure ($150 - 600$ m/s) down to 400 m depth could produce a significant traveltime delay of approximately 1 s in the shear-wave arrivals, which needs to be considered to avoid serious bias in shear-wave traveltime tomographic models.

INTRODUCTION

Marine engineering construction activities such as offshore oilfield and offshore wind power facilities require quantitative information of the site response at the ocean bottom, which is essential for reliable earthquake engineering design to mitigate hazards due to the strong ground motions from earthquakes in marginal seas such as the Bohai Sea of China (Figure 1a). The shear-wave velocity structures of sediments down to tens to hundreds of meters are important parameters for studies of site response (Wald and Mori, 2000; Boore, 2004; Boore et al., 2006) and have been investigated with various geotechnical and/or geophysical methods. The subocean shear-wave velocity structure of the shallow sediments also provides an effective proxy for evaluating the degree of consolidation for geotechnical applications, which can be used to predict the stability of foundations for marine engineering construction (Ayres and Theilen, 1999; Bohlen et al., 2004; Klein et al., 2005; Kugler et al., 2007). Moreover, reliable shear-wave velocity structure can also improve the tomography or imaging in offshore multicomponent seismic exploration (Bohlen et al., 2004; Kugler et al.,

Manuscript received by the Editor 6 August 2015; revised manuscript received 9 December 2015.
[1]Chinese Academy of Sciences, Institute of Geology and Geophysics, Key Laboratory of Petroleum Resources Research, and University of Chinese Academy of Sciences, Beijing, China. E-mail: ywang@mail.iggcas.ac.cn; xingjian@mail.iggcas.ac.cn; liulihua@mail.iggcas.ac.cn; lixuelei@mail.iggcas.ac.cn; hulitian@mail.iggcas.ac.cn.
[2]Chinese Academy of Sciences, Institute of Geodesy and Geophysics, State Key Laboratory of Geodesy and Earth's Dynamics, Wuhan, China. E-mail: zwli@whigg.ac.cn.
[3]Chinese Academy of Sciences, Institute of Geology and Geophysics, Key Laboratory of Petroleum Resources Research, Beijing, China. E-mail: qyyou0880@mail.iggcas.ac.cn; tyhao@mail.iggcas.ac.cn; zcl@mail.iggcas.ac.cn.
[4]AECOM, Los Angeles, California, USA. E-mail: paul.somerville@aecom.com.

2007). Due to the extremely low shear-wave velocity (200 – 300 m/s) compared with that in a normal crust model (approximately 3500 m/s), shallow suboceanic sediments may strongly bias shear-wave tomography of the deep crust and the upper mantle structure (Xu et al., 2007; Zhao et al., 2008, 2010; Xu et al., 2011; Li et al., 2012; Hao et al., 2013). For example, for sediments with shear-wave velocity of 300 m/s and thickness of 300 m, the traveltime delay for the shear-wave can be approximately 1 s. Altogether, the shear-wave velocity structure of suboceanic shallow sediments needs to be investigated for earthquake hazard mitigation and tomography studies.

Many studies involving invasive methods (e.g., borehole logging) and noninvasive geophysical methods (e.g., spectral analysis of surface-waves [SASW], multichannel analysis of surface waves [MASW], and refraction microtremor) have been used to investigate shallow onshore shear-wave velocity structures (Miller et al., 1999; Park et al., 1999; Louie, 2001; Murillo et al., 2009; Fernández et al., 2011; Goh et al., 2011; Nazarian, 2012; Parker and Hawman, 2012; Odum et al., 2013). With dense seismic receivers and array-based geophysical methods, high-resolution shear-wave velocity structures are obtained, which provide a basis for estimating the site response of the shallow sediments. Li et al. (2014) and Ni et al. (2014) obtain shear-wave velocity structure of shallow sediments beneath seismic stations with local earthquake waveforms. However, it is usually difficult to directly apply conventional onshore geophysical methods in the offshore environment, and so it is usually challenging to investigate the shallow shear-wave velocity structure of marine sediments. However, the development of ocean-bottom seismometers (OBSs) has led to their increasing use to study crust and upper mantle structure (Nakamura et al., 1987; Digranes et al., 1996; Flueh et al., 1998; Chian et al., 1999; Okaya et al., 2002; Parkin and White, 2008; Zhao et al., 2008; Zhao et al., 2010; Hao and You, 2011; Lü et al., 2011; Qiu et al., 2011; Clark et al., 2013; Klingelhoefer et al., 2014; Liu et al., 2015). The OBS investigations with dense active sources (e.g., air gun, electric spark) have also been conducted to invert for offshore shallow shear-wave velocity structure using high-quality surface-wave data (Shtivelman, 2003; Bohlen et al., 2004; Shtivelman, 2004; Klein et al., 2005; Kugler et al., 2006; Kugler et al., 2007; Nguyen et al., 2009; Socco et al., 2011; Vanneste et al., 2011; Dong et al., 2012).

Surface-wave dispersion has proved to be an effective tool for obtaining high-resolution shear-wave velocity structure of shallow sediments. An active air-gun source can excite strong surface waves recorded by seismometers even in marine environments. Another onshore and offshore active source for shallow shear-wave velocity study is the shear-wave vibrator, which can produce shear-waves in a fixed frequency range and obtain the higher modes of dispersion (Socco et al., 2011). The shot spacing can be conveniently adjusted when conducting the seismic data acquisition, which can greatly improve the lateral resolution of the shallow shear-wave structure (Bohlen et al., 2004; Klein et al., 2005; Kugler et al., 2007). Common receiver gathers (CRGs) are usually used to process the seismic waveform data along the shot line because the shot spacing can be changed more easily than the receiver interval (Bohlen et al., 2004). Seismic data acquisition systems such as OBS, ocean-bottom hydrophones, buried geophones, and towed streamer arrays are widely used to collect seismic signals from active sources (Ewing et al., 1992; Klein et al., 2005; Kugler et al., 2007; Hao and You, 2011).

In this study, seismic data from a 7C broadband OBS array and a large-volume air gun were used to investigate suboceanic shear-wave velocity in the Bohai Sea. Benefiting from the relative lower

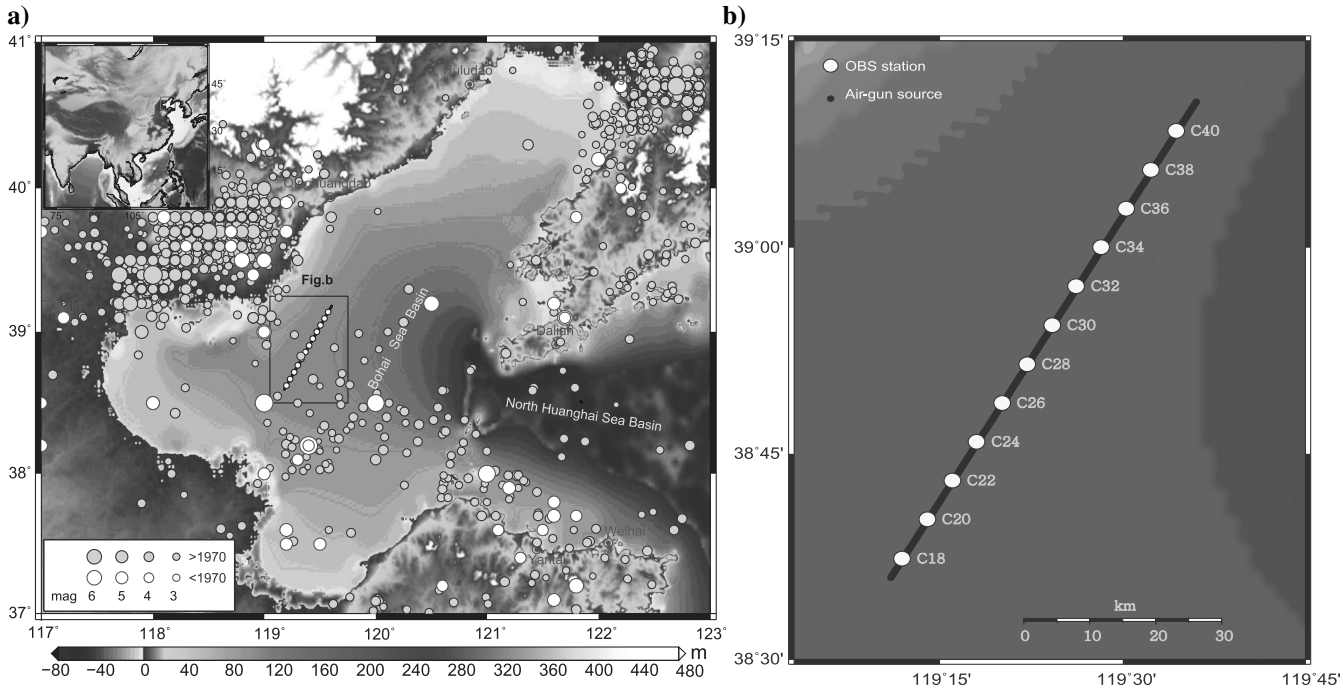

Figure 1. (a) Topography of the study area and the location of the survey line. The shot positions are denoted by black dots and the white dots indicate the OBS station positions. The gray and white circles are the earthquake epicenters. (b) The distribution of OBS stations and air-gun sources.

frequency band of the OBS and large-volume air gun, high signal-to-noise-ratio (S/N) surface waves within the offset 0.4–5 km were clearly recorded, enabling the development of a high-resolution shear-wave velocity structure beneath the survey line. The fundamental and first overtone dispersion curves of surface waves in the frequency band of 0.9–3.0 Hz were extracted by the phase-shift method and were used to invert for shear-wave velocity structure of the shallow sediments. Pseudo-2D shear-wave velocity profiles to approximately 400 m depth were constructed, which provide important information for offshore site response analysis and engineering in the Bohai Sea.

METHOD

The Scholte wave is generated as an interface wave that propagates along the liquid-solid interface (Rayleigh, 1885; Stoneley, 1924; Scholte, 1947; Flores-Mendez et al., 2012). When the water depth is much less than the wavelength, the Scholte wave can be approximated as a Rayleigh wave (Bohlen et al., 2004). In this study, the water depth is shallower than 20 m for all areas beneath the OBS survey line. The frequency band of the surface wave in this study is 0.9–3 Hz, which corresponds to wavelengths of 110–390 m for the typical ocean-bottom sediment shear velocity of 350 m/s. Therefore, the wavelength is 5–20 times the average water depth (i.e., 20 m), which suggests that the "Rayleigh-wave" approximation is valid (Park et al., 2005). Although the Scholte-wave data here could be processed as Rayleigh waves due to the shallow water and relatively long wavelength, we still included the 20 m thick water layer in the starting model for velocity inversion to minimize dispersion errors from the water layer.

Two methods are usually used to extract surface-wave dispersion curves from seismic recordings of active sources. The SASW approach uses two receivers at various distances to extract individual dispersion curves, and then it combines them to construct the final dispersion curve. It can retrieve the fundamental mode of the dispersion curve rapidly but underestimates the overtones. The quality control and phase unwrapping uncertainty problems that exist in the SASW method have been studied by many researchers (Nazarian, 2012). The MASW method uses many channels of surface-wave data to construct the fundamental and overtone dispersion curves. The raw surface-wave seismic data in the x-t (distance-time) domain is transformed into the frequency-velocity (f-v) or slowness-frequency (p-f) domain, and then the phase travel information is used to construct the dispersion energy image. Forbriger (2003) introduces the Fourier-Bessel transform to the full signal content. Xia et al. (2007) transform the x-t domain shot gathers into pseudovibroseis data or frequency-swept data by a frequency decomposition calculation, and they perform slant stacking to generate an f-v domain energy image. A high-resolution linear slant-stacking method is also used to improve the dispersion energy peak resolution and to separate different modes of the dispersion curve (Luo et al., 2008, 2009). Park et al. (1998) apply the Fourier transform to shot gathers followed by normalization, and then they perform the phase shift to generate a dispersion energy image in the f-v domain. Bohlen et al. (2004) also perform a Fourier transform to construct the dispersion energy in the f-p domain and apply the offset-dependent phase shift, with a Gaussian offset window applied to the original wavefield data before conducting the transform.

In this study, the phase-shift method is applied to the Fourier transform of the shot gathers after normalization, and it is used to obtain the dispersion energy image (Park et al., 1998, 2005). For N trace of seismic data r_i ($i = 1,2, \ldots, N$) in the x-t domain, the Fourier transform for each trace is given as:

$$R_i(\omega) = \mathrm{FFT}[r_i] = A_i(\omega) \cdot P_i(\omega), \tag{1}$$

where $A_i(\omega)$ denotes the amplitude at offset (x_i), which takes into account the effects of distance-dependent phase shifts due to attenuation and other frequency-dependent effects due to scattering in a heterogeneous structure. Moreover, it also contains the effect of phase shifts due to the source functions of the air-gun sources, which are manifested as constants in the amplitude normalization procedure; $P_i(\omega)$ is the phase term, which is determined by the phase velocity ($V_{\mathrm{ph}}[\omega]$),

$$P_i(\omega) = e^{-j(\omega x_i / V_{\mathrm{ph}}(\omega))} \tag{2}$$

$A_i(\omega)$ is removed by normalization:

$$R_{i,\mathrm{norm}}(\omega) = \frac{R_i(\omega)}{A_i(\omega)} = \frac{R_i(\omega)}{|R_i(\omega)|} = P_i(\omega). \tag{3}$$

The phase shift defines a trial phase-velocity range with small increments. The final dispersion energy spectrum in the f-v domain can be obtained by a summation operation as shown below:

$$P(V_{\mathrm{ph,range}}, \omega) = \frac{1}{N} \sum_{1}^{N} e^{j\left(\frac{\omega x_i}{V_{\mathrm{ph,test}}(\omega)}\right)} R_{i,\mathrm{norm}}(\omega); (i = 1,2, \ldots, N). \tag{4}$$

Because the phase velocity corresponds to the peak energy value for each frequency slice, the final dispersion curve can be obtained by picking all peak values within the defined frequency range from the dispersion energy image.

The shear-wave velocity structure inversion is conducted with multiple initial models with various numbers of layers and different thickness. The partial derivatives of the Scholte-wave phase-velocity dispersion with respect to the shear-wave velocities for each layer were calculated based on the initial 1D model. A damped iterative least-squares algorithm was used to solve the nonlinear inversion problem. The inversion was implemented using computer programs in seismology (CPS) (Herrmann, 2013). CPS has been widely used in surface-wave processes and shear-wave velocity inversion for shallow sediments, deep crust, and upper mantle structures, and it has proved to be an effective tool for velocity structure inversion.

SEISMIC DATA

A north-northeast–south-southwest-oriented OBS survey profile with a total length of approximately 70 km was conducted in the Bohai Sea, North China, in 2011 (Figure 1b). The average OBS receiver spacing was approximately 5 km. The average water depth along the survey profile was approximately 20 m. Twelve broadband (0.016–100 Hz) I-7C OBSs designed by the Institute of Geology and Geophysics, Chinese Academy of Sciences, were deployed in the Bohai Sea (Figure 2) (Hao and You, 2011). The OBS has been successfully used in many crustal structure studies in the South China Sea, Western Pacific, Indian Ocean, Bohai Sea, etc. (Hao and You, 2011; Lü et al., 2011; Qiu et al., 2011; Liu et al.,

Figure 2. The I-7C type OBS deployed in the survey in 2011. The instrument has seven components (including one hydrophone, one 3C broadband seismometer [0.016–100 Hz], and one 3C high-frequency seismometer [4.5–200 Hz], respectively). The maximum working water depth is 6000 m.

2012, 2015; Qiu et al., 2012; Ruan et al., 2012; Zhang et al., 2013). These surveys show that the OBS has good performance in data recording quality and instrument recovery (>98%) (Hao and You, 2011). An active-source 9000 in^3 air gun was shot at a depth of 5 m below sea level with an average interval distance of 190 m to each shot. The differential GPS technique was used for positioning and timing between the OBS and air gun.

For the clock drift correction, the timing calibrations are conducted twice by GPS when deploying and recovering the OBS assuming linear clock shift, which should be valid for a short experiment of two-week deployment. More advanced techniques for clock drift correction have been applied for long deployments (Sens-Schönfelder, 2008; Xia et al., 2015). Finally, 12 CRGs data groups were obtained from the raw vertical component data. The traces with offsets of less than approximately 400 m were cut for each CRG because the waveforms were clipped due to the strong energy near the source. To guarantee the high S/N of the surface-wave data, the maximum source-receiver offset was set to approximately 5000 m. Altogether, 24 traces were used to extract the Scholte-wave phase-velocity dispersion curves by the phase-shift method. We also tested different offsets (400–2200 m for the nearest offset and 4300–6000 m for the farthest offset) to construct dispersion images. We found that the dispersion images remained almost

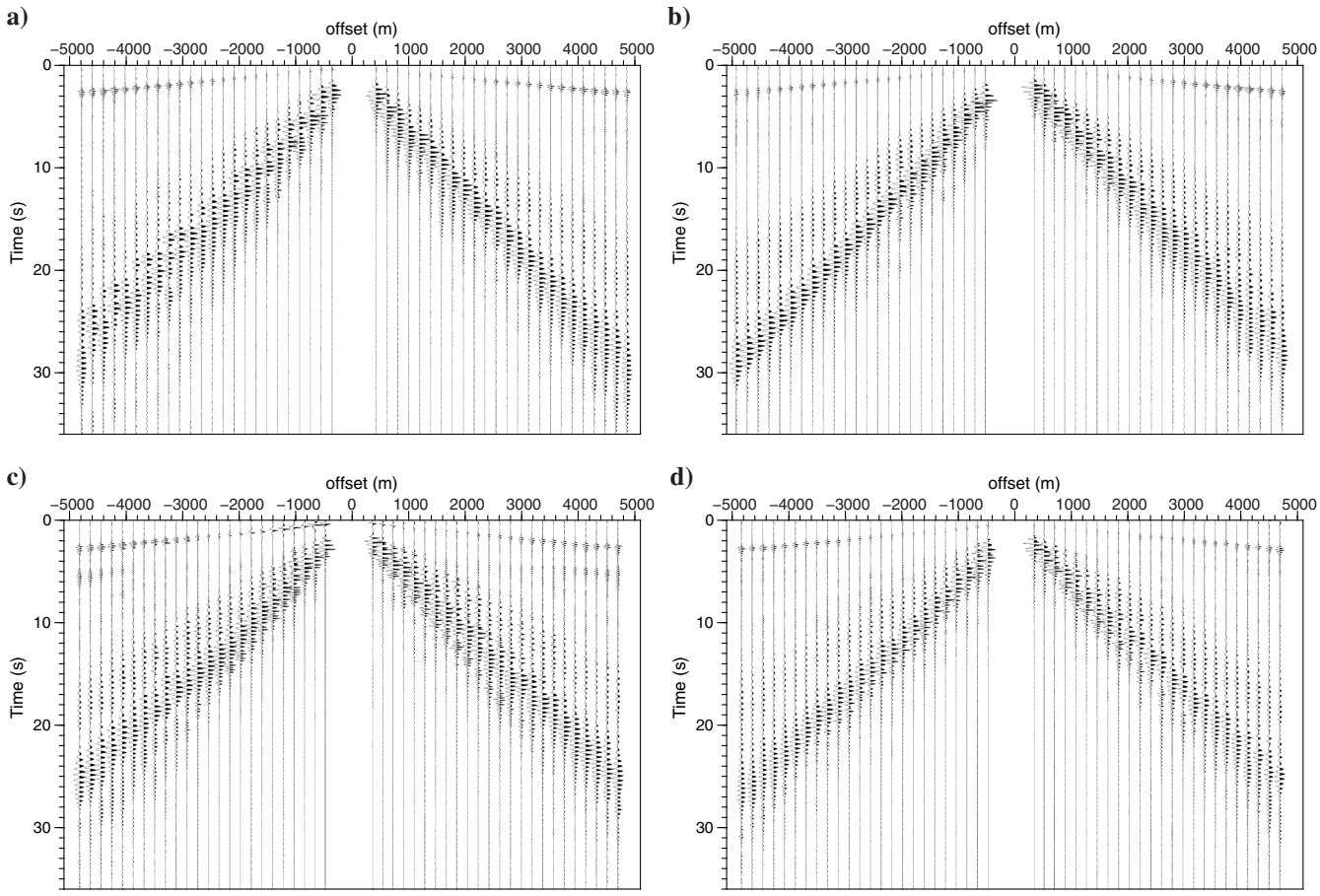

Figure 3. The CRG recorded by four OBS stations of (a) C30, (b) C32, (c) C38, and (d) C40. The mean value gain, 0.6–3 Hz band-pass filter, and rms gain were applied to each trace. The processed CRG seismogram shows a strong dispersive fundamental mode Scholte wave.

the same, although there was a slight difference at the low-frequency end, which could be due to the near-field surface effect. However, we retained 400 m for the nearest offset because waveforms at this distance still meet far-field requirements at the high-frequency end. A band-pass filter of 0.6–4 Hz and amplitude normalization were implemented for each trace to improve the S/N of the Scholte wave. After the data preprocessing, all of the CRGs showed high S/N Scholte waves (Figure 3). Due to the large-volume air gun, the seismograms showed strong Scholte wave at offsets up to approximately 5 km.

RESULTS

Twenty-four Scholte-wave dispersion curves were extracted from the left and right sides of the 12 CRGs by the phase-shift method, which actually samples the averaged velocity structure beneath each segment. The energy images for extracting the phase-velocity dispersions are shown in the frequency-velocity domain (Figure 4). As shown in Figure 4, the fundamental and first overtone can clearly be identified. High-resolution fundamental mode Scholte-wave dispersion curves are clearly shown between 0.9 and 2.9 Hz with strong amplitudes, sharp peaks, and good continuity. The first overtone dispersion curves can also be identified between 1.2 and 2.2 Hz. However, the energy amplitude and resolution is somewhat lower than for the fundamental mode. All dispersion curves for all data sets are characterized by similar trends with a maximum difference of approximately 50 m/s. The fundamental mode Scholte-wave phase velocity varies from 200 to 450 m/s, and the first overtone Scholte-wave phase velocity varies from 350 to 550 m/s.

Twenty-four Scholte-wave phase-velocity dispersion curves and six trial models with 9–25 layers to 500 m were used to conduct the trial inversions. The 1D P-wave velocity model from fitting the first P arrivals was used in the inversion (Figure 5). All measured dispersion curves could be fitted very well in different trials (Figure 6). Moreover, all final shear-wave velocity models showed high similarity even though the layer numbers and thicknesses are different. Finally, 24 1D shear-wave velocity models were derived from the inversion of 24 Scholte-wave phase-velocity dispersion curves. The

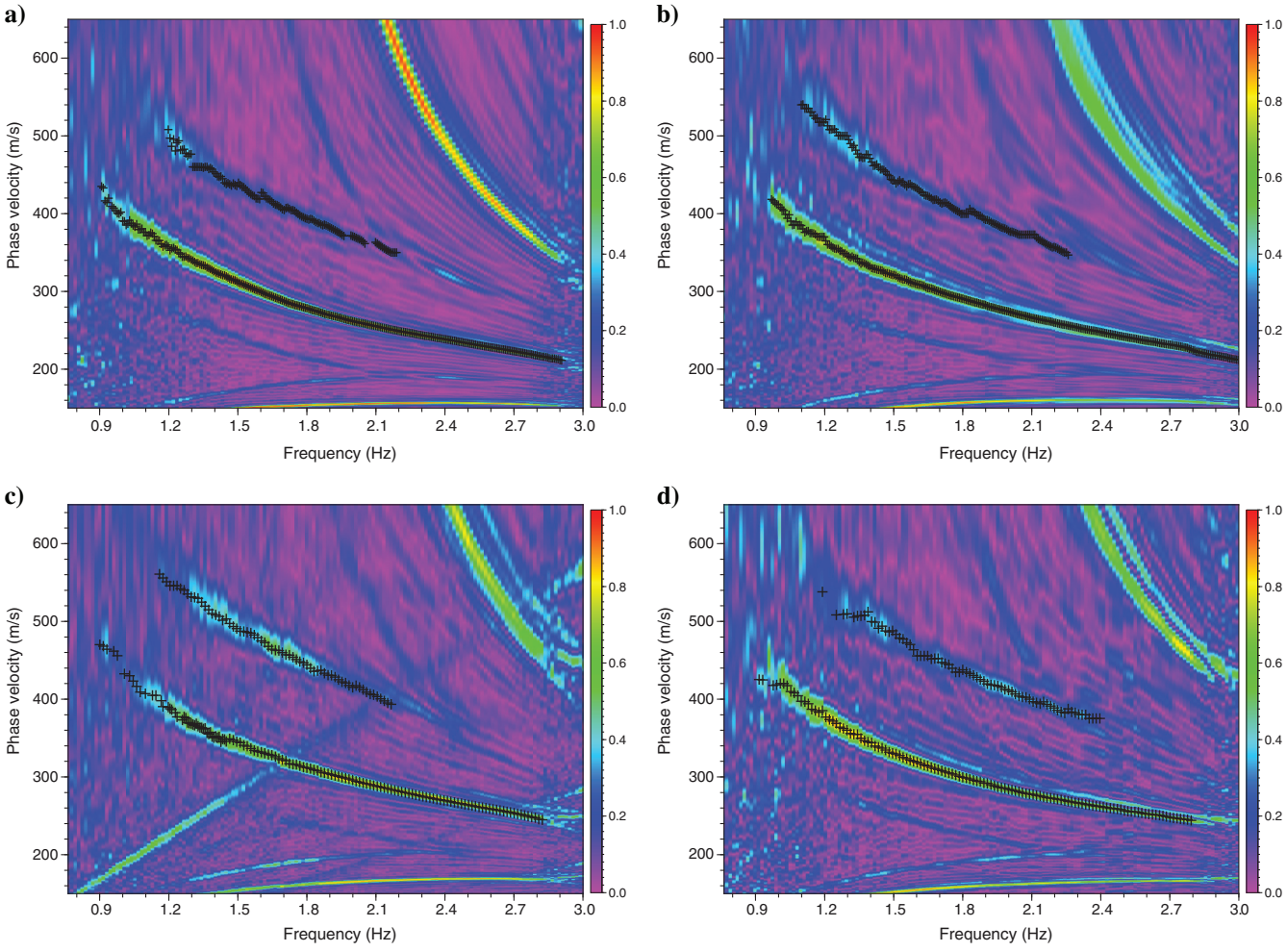

Figure 4. The dispersion energy images in the f-v domain generated by the phase-shift method and the dispersion curves picked from the energy peak (denotes with the black cross). The dispersion energy was calculated using the right (positive offset value) branches of the CRG seismograms shown in Figure 3. The dispersion energy images shown in (a-d) correspond to the right branches of the CRGs shown in Figure 3a–3d, respectively.

shear-wave sensitivity kernels of the Scholte-wave phase velocity suggest that the shear-wave velocity structure to a 300 m depth can be well-constrained by the dispersion curves at 1–3 Hz. For the deeper depth range of 300–400 m, the fundamental and first overtone Scholte-wave phase-velocity dispersion curves at 1 Hz still provide some constraints on the shear-wave velocity structure (Figure 7). Therefore, the shear-wave velocity structures to 400 m depth were presented as the final results.

With 24 1D shear-wave velocity models from different initial models, pseudo-2D shear-wave velocity structure profiles beneath the OBS survey line were obtained by linear interpolation, in which each 1D model is set to the middle position of its CRGs (Figure 8). shear-wave velocities of 150 300 m/s are shown for depths less than 100 m. Down to a 200 m depth, the shear-wave velocity increases to 300 500 m/s. For the depth range of 300–400 m, the shear-wave velocities are approximately 500 700 m/s. Although different initial models with different layers and velocities were used in the inversions, similar characteristics and weak lateral velocity contrasts are seen in the 2D velocity profiles.

DISCUSSION

The shear-wave velocity structure can be inverted using the fundamental and first overtone dispersion curves of the Scholte wave. Joint inversion of the fundamental and overtone dispersion can provide further constraints on the deeper structure and also improve the resolution of the shallow structure (Xia et al., 2003; Luo et al., 2007). Scholte-wave dispersion is mostly sensitive to the shear-wave velocity and is affected weakly by the P-wave velocity and density. In this study, only the shear-wave velocity was taken as unknown, with P-wave velocity and density fixed in the inversion. With the first P-wave arrivals, a two-layer 1D P-wave model was constructed by fitting the first P-wave arrivals with the grid-search method (Figure 5). The optimized results suggest that the P-wave velocity varies between 1750 and 2200 m/s in the survey area, and a two-layer model can fit the first P-wave arrivals very well, which has small residuals (<0.05 s) between the measured and synthetic first P-wave arrivals. The density structure was then calculated based on the empirical relationships between the P-wave velocity and the density (Gardner et al., 1974; Christensen and Mooney, 1995).

To minimize the effects of the initial model in the linear inversion, six different starting models with different numbers and thickness of layers were used. Relatively small differences were found in the inverted results (Figure 8). The uncertainty of the inverted shear-wave velocity structure was also estimated from the standard deviation of the six pseudo-2D profiles from six trial inversions with different initial models (Figure 9). These results suggest that the shear-wave velocity uncertainty is 5 20 m/s for most areas of the 2D profile, which is approximately 2%–6% for an average shear-wave velocity of 300 m/s. For some portion of the survey

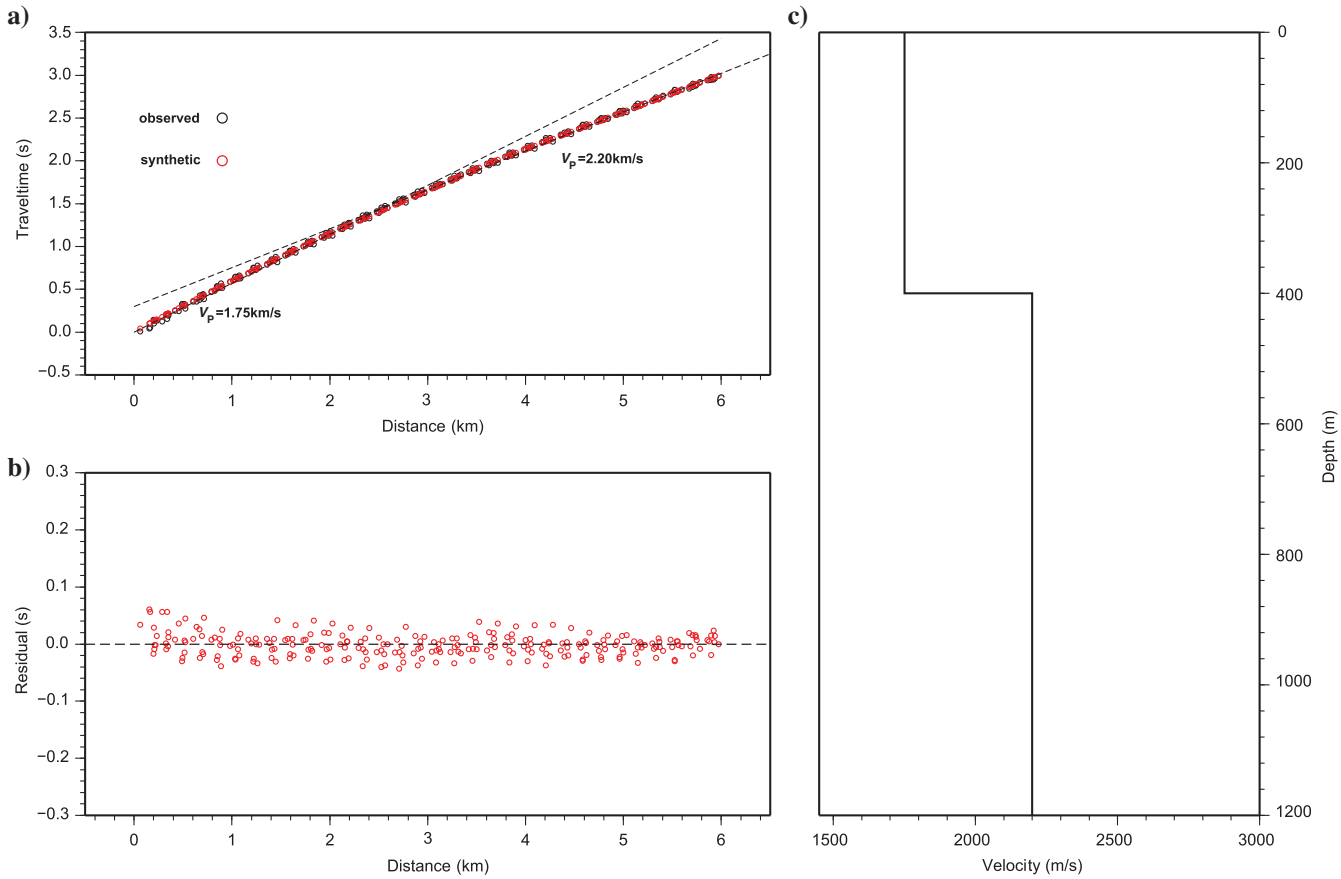

Figure 5. (a) The measured and synthetic first P-wave traveltime. The two dashed lines represent the traveltime with P-wave velocities of 1750 and 2200 m/s. (b) Residuals between the measured and synthetic results. (c) The final two-layer P-wave velocity model.

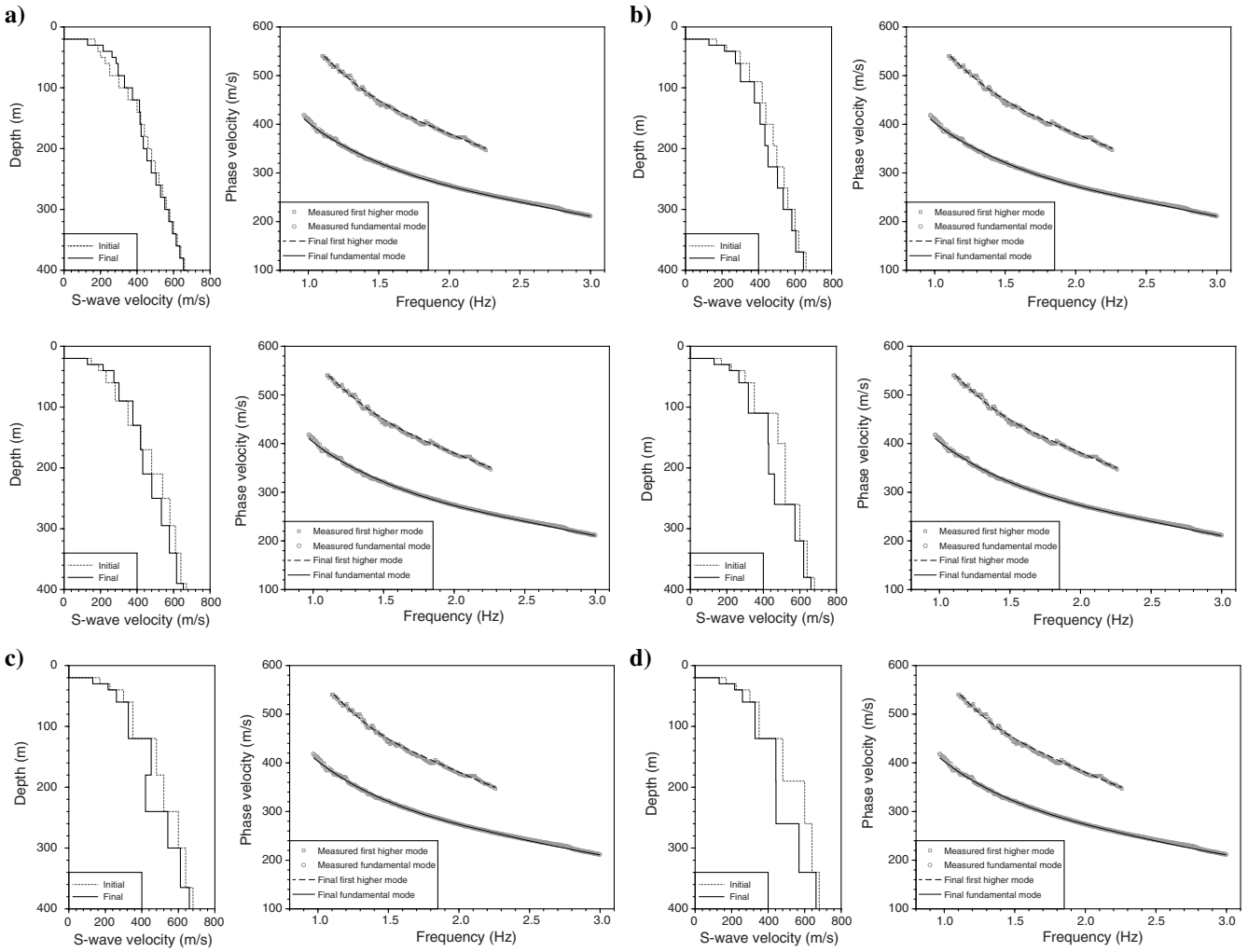

Figure 6. Each panel includes two parts: The left side shows the initial (dashed line) and inverted (solid line) 1D shear-wave velocity model. The right side shows the measured (black pattern, Figure 4b) and calculated (black solid line) dispersion curves with respect to the final inverted model. During the inversion, we jointly inverted the fundamental mode and first overtone simultaneously by a linear inversion method with six initial models. The panels (a-f) show all of the six initial models and their inverted results and indicate that all of the initial models fit the observed dispersion curves very well.

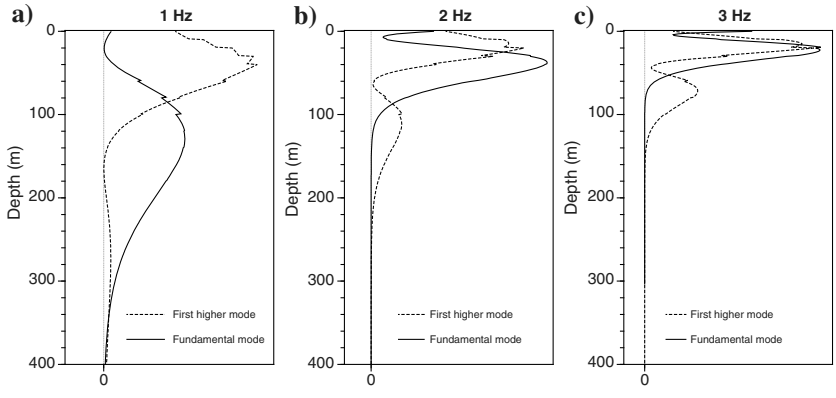

Figure 7. The shear-wave velocity sensitivity kernels of the fundamental and first overtone Scholte-wave phase velocity at different frequencies.

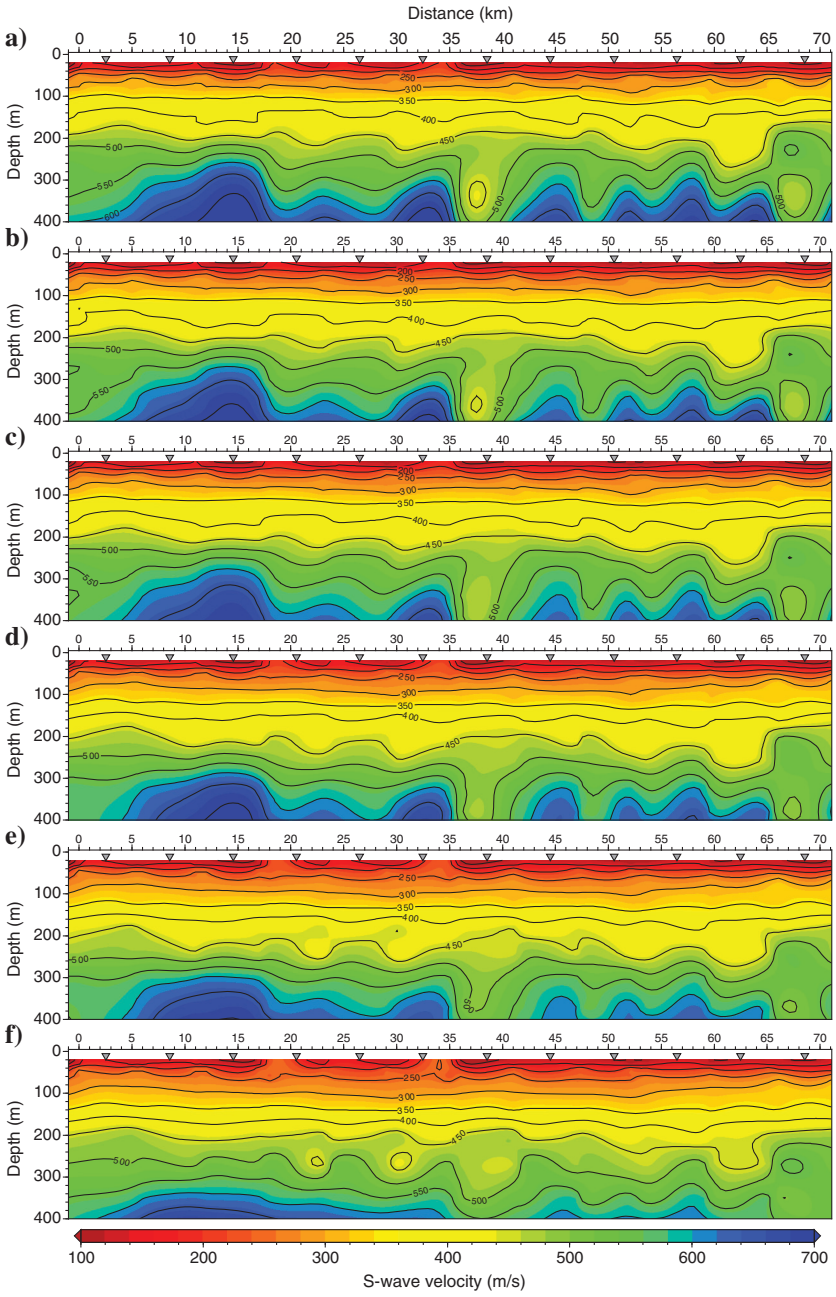

Figure 8. The final 2D shear-wave velocity profile inverted from different initial models (Figure 6a–6f). The profile is plotted along the shot line, and the OBSs are denoted by inverted triangles.

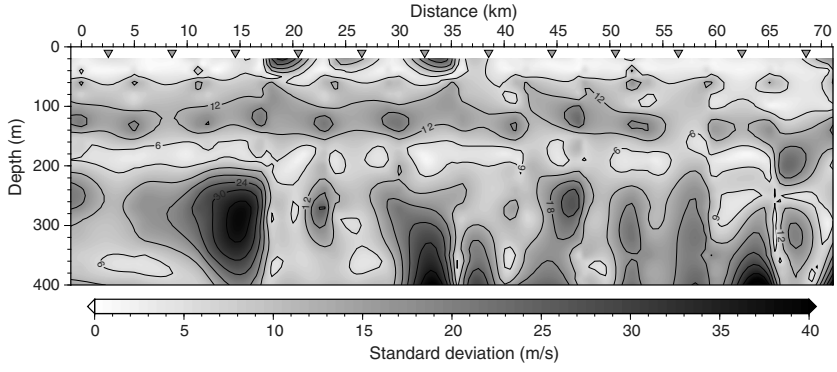

Figure 9. Standard deviations based on six 2D shear-wave velocity profiles are shown in Figure 8.

line, the uncertainties in the shear-wave velocity can reach up to 40 m/s, approximately 13% of the background velocity.

Based on the pseudo-2D shear-wave velocity profiles, weak lateral heterogeneities were observed for the shear-wave velocity structure from shallow depths to depths of 400 m. The average shear-wave velocity along the shot line was calculated from 24 1D inversion results with different initial models (Figure 10). The average shear-wave velocity along the survey line was also calculated from the six 2D shear-wave velocity profiles (Figure 11). The average value changed from 150 to 610 m/s from the seabed to 400 m depth with a small variation gradient in this area. The standard deviations vary from approximately 20 to 50 m/s from shallow to deeper depths. The weak lateral variation in shear-wave velocity may be attributable to the continuous and stable sedimentary environment and the large sediment thickness in the Cenozoic sedimentary basin of Bohai Bay basin (Hao et al., 2007; Hou and Hari, 2014; Liu et al., 2015). The maximum Cenozoic sediment thickness is up to approximately 10 km in the Bohai Sea, and the pre-Cenozoic sediment thickness is greater than 5 km (Hao et al., 2007; Xu et al., 2007). It should be noted that the final 2D shear-wave velocity structure is not a real 2D inversion results. Due to the relatively small lateral variation in the shallow sediments in the Bohai Sea, the approximation of constructing the pseudo-2D shear-wave velocity structure from 1D models was appropriate for depicting the 2D structure. Full-waveform inversion of surface waves would be a more accurate way of modeling the 2D shear-wave velocity structure.

In the above analysis, we adopt a simple two-layer P-wave velocity and constant density model. To explore the effects of different P-wave velocities and density models on the shear-wave velocity inversion, we invert dispersion curves assuming a more realistic model, which involves a linearly increasing P-wave velocity with depth, as expected from increasing pressure and compaction (Brocher, 2008). The density was calculated from empirical relations between the P-wave velocity and the density. The results show that with different starting P-wave velocity and density models, the inverted shear-wave velocity models remain very stable (Figure 12), suggesting that the P-wave velocity and density models do not have obvious effects on the shear-wave velocity inversion.

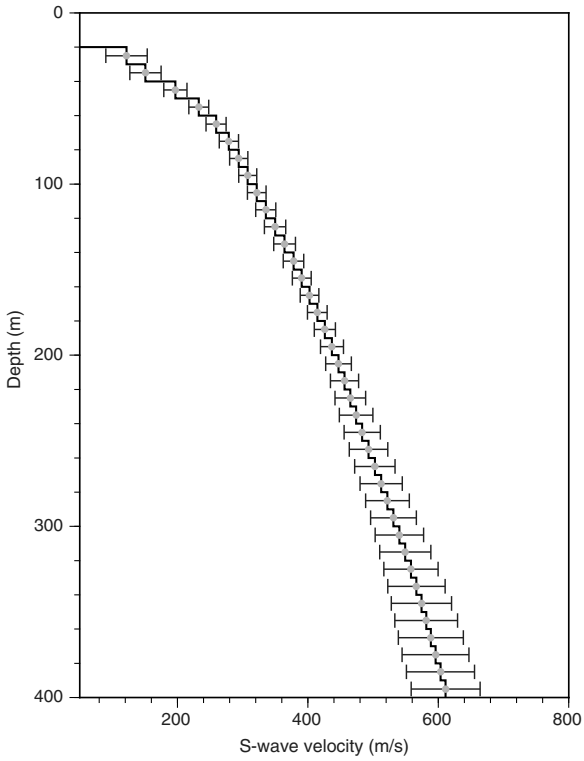

Figure 11. The average shear-wave velocity calculated from six 2D shear-wave velocity profiles shown in Figure 8. The error bars show the standard deviations.

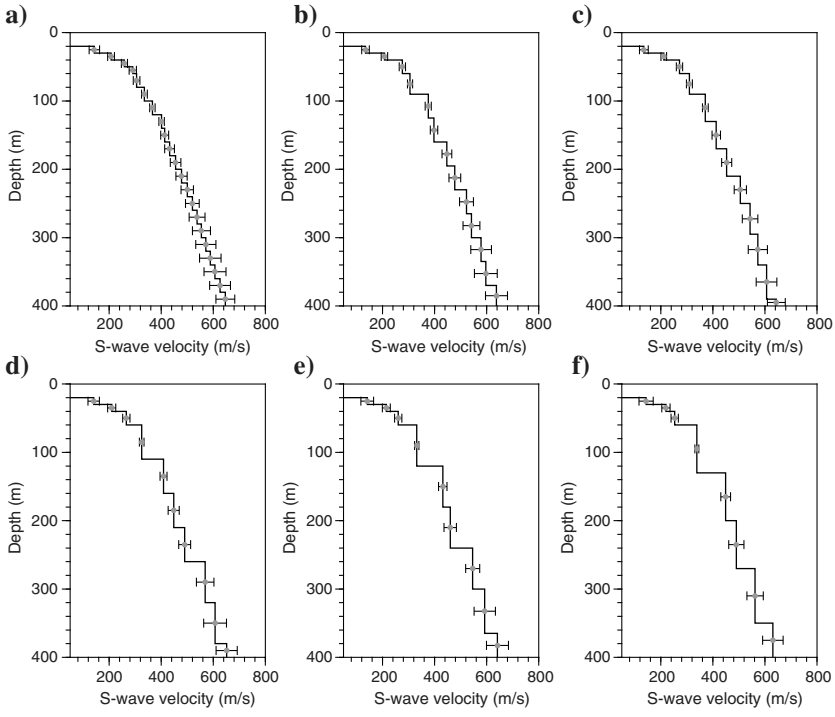

Figure 10. The average value of the shear-wave velocity (black solid line) calculated from 24 1D inverted shear-wave velocity profiles. (a-f) Six inverted shear-wave velocity profiles were developed with different initial models (Figure 8a–8f). The error bars represent the standard deviations of the shear-wave velocity.

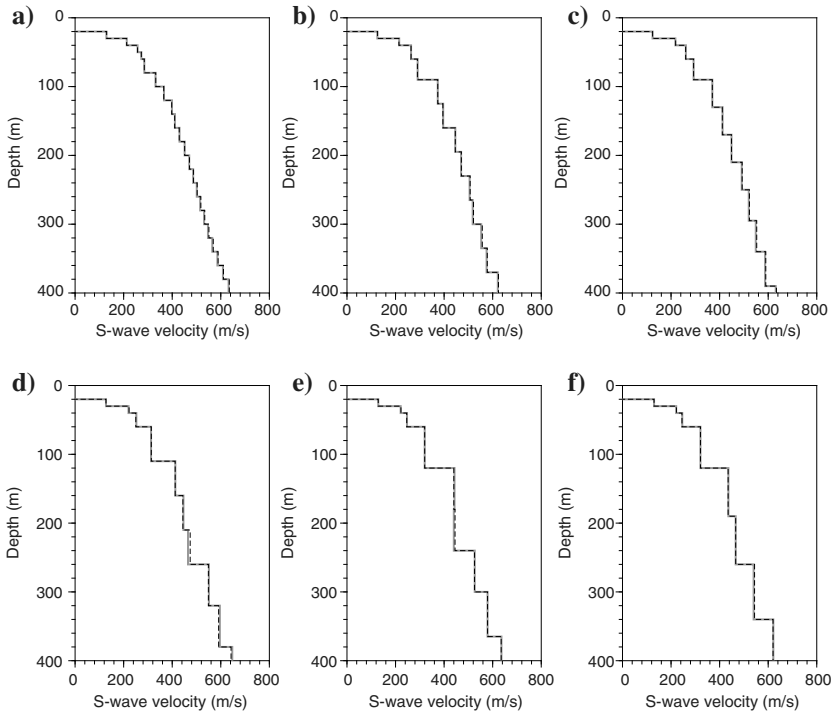

Figure 12. Comparisons between the inverted shear-wave velocity models with different starting models of P-wave velocity and density. Panels (a-f) correspond to the inverted models shown in Figure 6a–6f, respectively. Gray solid lines indicate the inverted shear-wave velocity models from starting models with linearly increasing P-wave velocity and density models with depth (Brocher, 2008). The density is calculated from empirical relations between the P-wave velocity and the density. The black dashed lines indicate the model inverted from the original starting model with two-layer P-wave velocity and constant density as shown in Figure 6.

CONCLUSION

The shallow shear-wave velocity structure is of interest in studies of onshore and offshore engineering because it can provide important information on site response. Because common onshore subsurface shear-wave velocity investigation methods cannot be directly used in offshore areas, surface-wave data from an OBS survey with air-gun sources were used to estimate the shallow shear-wave velocity in the Bohai Sea (Bohai Bay Basin), North China. High-quality surface-wave dispersion curves were extracted from an approximately 70 km long seismic survey line including 12 OBSs and 377 shots from a 9000 in^3 air gun. The shear-wave velocity structure of the shallow sediments beneath the seabed was inverted using a damped iterative least-squares inversion scheme for Scholte-wave dispersion curves in the 0.9–3.0 Hz frequency range. Pseudo-2D shear-wave velocity profiles down to an approximately 400 m depth below the ocean bottom along the OBS survey line suggest similar characteristics and weak lateral velocity contrasts, which may be attributable to the continuous sedimentary environment in the Cenozoic sedimentary basin of the Bohai Bay Basin. Shear-wave velocities of 150 300 m/s were found for the shallow 100 m depth. Down to a 200 m depth, the shear-wave velocity increases to 300 500 m/s. For the depth range of 300–400 m, the shear-wave velocities are approximately 500 700 m/s. Low shear-wave velocities of 200 300 m/s at the shallow depth of 100 m were found beneath the survey line, which could provide important information for offshore site response analysis and engineering.

ACKNOWLEDGMENTS

We would like to thank the editor, J. Etgen, and three anonymous reviewers for their valuable comments that greatly improved the manuscript. We also thank S. Ni for his very helpful comments on this study. We thank all the investigators and crew members on the ships *Xiangyanghong 8* and *Fendou 7* for collecting the seismic data. This research is supported by ZDYZ2012-1-08, 2013YQ120357, NSFC (41210005, 41476033, 41404050, 41304079, 90814011), XDB06030203, 2013CB733204, and Youth Innovation Promotion Association Chinese Academy of Sciences.

REFERENCES

Ayres, A., and F. Theilen, 1999, Relationship between P- and S-wave velocities and geological properties of near-surface sediments of the continental slope of the Barents Sea: Geophysical Prospecting, **47**, 431–441, doi: 10.1046/j.1365-2478.1999.00129.x.

Bohlen, T., S. Kugler, G. Klein, and F. Theilen, 2004, 1.5D inversion of lateral variation of Scholte-wave dispersion: Geophysics, **69**, no. 2, 330–344, doi: 10.1190/1.1707052.

Boore, D. M., 2004, Ground motion in Anchorage, Alaska, from the 2002 Denali fault earthquake: Site response and displacement pulses: Bulletin of the Seismological Society of America, **94**, S72–S84, doi: 10.1785/0120040606.

Boore, D. M., J. Watson-Lamprey, and N. A. Abrahamson, 2006, Orientation-independent measures of ground motion: Bulletin of the Seismological Society of America, **96**, 1502–1511, doi: 10.1785/0120050209.

Brocher, T. M., 2008, Compressional and shear-wave velocity versus depth relations for common rock types in northern California: Bulletin of the Seismological Society of America, **98**, 950–968, doi: 10.1785/0120060403.

Chian, D. P., K. E. Louden, T. A. Minshull, and R. B. Whitmarsh, 1999, Deep structure of the ocean-continent transition in the southern Iberia Abyssal Plain from seismic refraction profiles: Ocean Drilling Program (Legs 149 and 173) Transect: Journal of Geophysical Research, **104**, 7443–7462, doi: 10.1029/1999JB900004.

Christensen, N. I., and W. D. Mooney, 1995, Seismic velocity structure and composition of the continental crust: A global view: Journal of Geophysical Research, **100**, 9761–9788, doi: 10.1029/95JB00259.

Clark, S. A., J. I. Faleide, J. Hauser, O. Ritzmann, R. Mjelde, J. Ebbing, H. Thybo, and E. Flüh, 2013, Stochastic velocity inversion of seismic reflection/refraction traveltime data for rift structure of the southwest Barents Sea: Tectonophysics, **593**, 135–150, doi: 10.1016/j.tecto.2013.02.033.

Digranes, P., R. Mjelde, S. Kodaira, H. Shimamura, T. Kanazawa, H. Shiobara, and E. W. Berg, 1996, Modelling shear waves in OBS data from the Northern Norway by 2-D ray-tracing: Pure and Applied Geophysics, **147**, 611–629, doi: 10.1007/BF01089694.

Dong, H., T. D. Nguyen, and K. Duffaut, 2012, Estimation of shear-velocity profiles using shear source data in marine environment: The Journal of the Acoustical Society of America, **131**, 3278–3278, doi: 10.1121/1.4708258.

Ewing, J., J. A. Carter, G. H. Sutton, and N. Barstow, 1992, Shallow water sediment properties derived from high-frequency shear and interface waves: Journal of Geophysical Research, **97**, 4739–4762, doi: 10.1029/92JB00180.

Fernández, J., L. Hermanns, A. Fraile, E. Alarcón, and I. Del Rey, 2011, Spectral-analysis-surface-waves-method in ground characterization: Procedia Engineering, **10**, 3202–3207, doi: 10.1016/j.proeng.2011.04.529.

Flores-Mendez, E., M. Carbajal-Romero, N. Flores-Guzmán, R. Sánchez-Martínez, and A. Rodríguez-Castellanos, 2012, Rayleigh's, Stoneley's, and Scholte's interface waves in elastic models using a boundary element method: Journal of Applied Mathematics, **2012**, 1–15, doi: 10.1155/2012/313207.

Flueh, E. R., M. A. Fisher, J. Bialas, J. R. Childs, D. Klaeschen, N. Kukowski, T. Parsons, D. W. Scholl, U. T. Brink, A. M. Tréhu, and N. Vidal, 1998, New seismic images of the Cascadia subduction zone from cruise

SO108 — Orwell: Tectonophysics, **293**, 69–84, doi: 10.1016/S0040-1951(98)00091-2.
Forbriger, T., 2003, Inversion of shallow-seismic wavefields: I. Wavefield transformation: Geophysical Journal International, **153**, 719–734, doi: 10.1046/j.1365-246X.2003.01929.x.
Gardner, G. H. F., L. W. Gardner, and A. R. Gregory, 1974, Formation velocity and density: The diagnostic basics for stratigraphic traps: Geophysics, **39**, 770–780, doi: 10.1190/1.1440465.
Goh, T. L., A. R. Samsudin, and A. G. Rafek, 2011, Application of spectral analysis of surface wave method for rock mass characterization: Environment and Engineering Geoscience, **17**, 77–84, doi: 10.2113/gseegeosci.17.1.77.
Hao, T., C. Yang, H. Liu, H. Song, and W. Jiang, 2007, Integrated geological and geophysical study for pre-Cenozoic hydrocarbon resources in the circum-Bohai area (in Chinese): Progress in Geophysics, **22**, 1269–1279, doi: 10.3969/j.issn.1004-2903.2007.04.037.
Hao, T., and Q. You, 2011, Progress of homemade OBS and its application on ocean bottom structure survey (in Chinese): Chinese Journal of Geophysics, **54**, 3352–3361, doi: 10.3969/j.issn.0001-5733.2011.12.033.
Hao, T., Q. You, L. Liu, C. Lv, Y. Xu, Z. Li, C. Zhao, Y. Zheng, C. Liu, and G. Han, 2013, Joint land-sea seismic survey and research on the deep structures of the Bohai Sea areas: Acta Oceanologica Sinica, **32**, 13–24, doi: 10.1007/s13131-013-0383-4.
Herrmann, R. B., 2013, Computer programs in seismology: An evolving tool for instruction and research: Seismological Research Letters, **84**, 1081–1088, doi: 10.1785/0220110096.
Hou, G. T., and K. R. Hari, 2014, Mesozoic-Cenozoic extension of the Bohai Sea: Contribution to the destruction of North China Craton: Frontiers of Earth Science, **8**, 202–215, doi: 10.1007/s11707-014-0413-3.
Klein, G., T. Bohlen, F. Theilen, S. Kugler, and T. Forbriger, 2005, Acquisition and inversion of dispersive seismic waves in shallow marine environments: Marine Geophysical Researches, **26**, 287–315, doi: 10.1007/s11001-005-3725-6.
Klingelhoefer, F., M. Evain, A. Afilhado, C. Rigoti, A. Loureiro, D. Alves, A. Leprêtre, M. Moulin, P. Schnurle, M. Benabdellouahed, A. Baltzer, M. Rabineau, A. Feld, A. Viana, and D. Aslanian, 2014, Imaging proto-oceanic crust off the Brazilian Continental Margin: Geophysical Journal International, **200**, 471–488, doi: 10.1093/gji/ggu387.
Kugler, S., T. Bohlen, S. Bussat, and G. H. Klein, 2006, Variability of Scholte-wave dispersion in shallow-water marine sediments: Journal of Environmental and Engineering Geophysics, **10**, 203–218, doi: 10.2113/JEEG10.2.203.
Kugler, S., T. Bohlen, T. Forbriger, S. Bussat, and G. Klein, 2007, Scholte-wave tomography for shallow-water marine sediments: Geophysical Journal International, **168**, 551–570, doi: 10.1111/j.1365-246X.2006.03233.x.
Li, S., Y. Suo, L. Dai, L. Liu, C. Jin, X. Liu, T. Hao, L. Zhou, J. Zhou, and Q. Jiao, 2010, Development of the Bohai Bay Basin and destruction of the North China Craton: Earth Science Frontiers, **17**, 64–89.
Li, X., Y. Pei, B. Liu, Y. Zhao, C. Liu, Q. Xie, Q. Hua, and S. Deng, 2009, Acoustic detection of the causative fault of 1969 Ms 7.4 earthquake in Bohai Sea (in Chinese): Chinese Journal of Geophysics, **52**, 2291–2301, doi: 10.3969/j.issn.0001-5733.2009.09.013.
Li, Z. W., S. D. Ni, T. Y. Hao, Y. Xu, and S. Roecker, 2012, Uppermost mantle structure of the eastern margin of the Tibetan plateau from interstation Pn traveltime difference tomography: Earth and Planetary Science Letters, **335–336**, 195–205, doi: 10.1016/j.epsl.2012.05.005.
Li, Z. W., S. D. Ni, and P. Somerville, 2014, Resolving shallow shear-wave velocity structure beneath station CBN by waveform modeling of the Mw 5.8 mineral, Virginia, earthquake sequence: Bulletin of the Seismological Society of America, **104**, 944–952, doi: 10.1785/0120130190.
Liu, L., T. Hao, C. Lü, Q. You, J. Pan, F. Wang, Y. Xu, C. Zhao, and J. Zhang, 2015, Crustal structure of Bohai Sea and adjacent area (North China) from two onshore-offshore wide-angle seismic survey lines: Journal Asian Earth Sciences, **98**, 457–469, doi: 10.1016/j.jseaes.2014.11.034.
Liu, L., C. Lü, T. Hao, Q. You, Y. Zheng, P. Zhi, J. Pan, and S. Liu, 2012, Data processing methods of OBS and its development tendency in detection of offshore oil and gas resources (in Chinese): Progress in Geophysics, **27**, 2673–2684, doi: 10.6038/j.issn.1004-2903.2012.06.047.
Louie, J. N., 2001, Faster, better: Shear-wave velocity to 100 meters depth from refraction microtremor arrays: Bulletin of the Seismological Society of America, **91**, 347–364, doi: 10.1785/0120000098.
Lü, C., T. Hao, X. Qiu, M. Zhao, and Q. You, 2011, Deep crustal structure of the northern part of southwest sub-basin, South China Sea, from ocean bottom seismic data: Chinese Journal of Geophysics, **54**, 1022–1032, doi: 10.1002/cjg2.1681.
Luo, Y., J. Xia, J. Liu, Q. Liu, and S. Xu, 2007, Joint inversion of high-frequency surface waves with fundamental and higher modes: Journal of Applied Geophysics, **62**, 375–384, doi: 10.1016/j.jappgeo.2007.02.004.
Luo, Y., J. Xia, R. D. Miller, Y. Xu, J. Liu, and Q. Liu, 2008, Rayleigh-wave dispersive energy imaging using a high-resolution linear Radon transform: Pure and Applied Geophysics, **165**, 903–922, doi: 10.1007/s00024-008-0338-4.
Luo, Y., J. Xia, R. D. Miller, Y. Xu, J. Liu, and Q. Liu, 2009, Rayleigh-wave mode separation by high-resolution linear Radon transform: Geophysical Journal International, **179**, 254–264, doi: 10.1111/j.1365-246X.2009.04277.x.
Miller, R. D., J. Xia, C. B. Park, and J. M. Ivanov, 1999, Multichannel analysis of surface waves to map bedrock: The Leading Edge, **18**, 1392–1396, doi: 10.1190/1.1438226.
Murillo, C. A., L. Thorel, and B. Caicedo, 2009, Spectral analysis of surface waves method to assess shear wave velocity within centrifuge models: Journal of Applied Geophysics, **68**, 135–145, doi: 10.1016/j.jappgeo.2008.10.007.
Nakamura, Y., P. L. Donoho, P. H. Roper, and P. M. McPherson, 1987, Large-offset seismic surveying using ocean-bottom seismographs and air guns: Instrumentation and field technique: Geophysics, **52**, 1601–1611, doi: 10.1190/1.1442277.
Nazarian, S., 2012, Shear wave velocity profiling with surface wave methods, *in* K. Rollins, and D. Zekkos, eds., Geotechnical Engineering State of the Art and Practice: Keynote Lectures from GeoCongress 2012, 221–240, doi: 10.1061/9780784412138.
Nguyen, X. N., T. Dahm, and I. Grevemeyer, 2009, Inversion of Scholte wave dispersion and waveform modeling for shallow structure of the Ninetyeast Ridge: Journal of Seismology, **13**, 543–559, doi: 10.1007/s10950-008-9145-8.
Ni, S. D., Z. W. Li, and P. Somerville, 2014, Estimating subsurface shear velocity with radial to vertical ratio of local P waves: Seismological Research Letters, **85**, 82–90, doi: 10.1785/0220130128.
Odum, J. K., W. J. Stephenson, R. A. Williams, and C. von Hillebrandt-Andrade, 2013, V_{S30} and spectral response from collocated shallow, active-, and passive-source V_S data at 27 sites in Puerto Rico: Bulletin of the Seismological Society of America, **103**, 2709–2728, doi: 10.1785/0120120349.
Okaya, D., S. Henrys, and T. Stern, 2002, Double-sided onshore-offshore seismic imaging of a plate boundary: "Super-gathers" across South Island, New Zealand: Tectonophysics, **355**, 247–263, doi: 10.1016/S0040-1951(02)00145-2.
Park, C. B., R. D. Miller, and J. Xia, 1998, Imaging dispersion curves of surface waves on multi-channel record: 68th Annual International Meeting, SEG, Expanded Abstracts, 1377–1380.
Park, C. B., R. D. Miller, and J. Xia, 1999, Multichannel analysis of surface waves: Geophysics, **64**, 800–808, doi: 10.1190/1.1444590.
Park, C. B., R. D. Miller, J. Xia, J. Ivanov, G. V. Sonnichsen, J. A. Hunter, R. L. Good, R. A. Burns, and H. Christian, 2005, Underwater MASW to evaluate stiffness of water-bottom sediments: The Leading Edge, **24**, 724–728, doi: 10.1190/1.1993267.
Parker, E. H., and R. B. Hawman, 2012, Multi-channel analysis of surface waves (MASW) in karst terrain, Southwest Georgia: Implications for detecting anomalous features and fracture zones: Journal of Environmental and Engineering Geophysics, **17**, 129–150, doi: 10.2113/JEEG17.3.129.
Parkin, C. J., and R. S. White, 2008, Influence of the Iceland mantle plume on oceanic crust generation in the North Atlantic: Geophysical Journal International, **173**, 168–188, doi: 10.1111/j.1365-246X.2007.03689.x.
Qiu, X., M. Zhao, W. Ao, C. Lü, T. Hao, Q. You, A. Ruan, and J. Li, 2011, OBS survey and crustal structure of the Southwest Sub-basin and Nansha Block, South China Sea (in Chinese): Chinese Journal of Geophysics, **54**, 3117–3128, doi: 10.1002/cjg2.1680.
Qiu, X., M. Zhao, H. Xu, J. Li, A. Ruan, T. Hao, and Q. You, 2012, Important processes of deep seismic surveys in the South China Sea: Retrospection and expectation (in Chinese): Journal of Tropical Oceanography, **31**, 1–9, doi: 10.3969/j.issn.1009-5470.2012.03.001.
Rayleigh, L., 1885, On waves propagated along the plane surface of an elastic solid: Proceedings of the London Mathematical Society, **s1-17**, 4–11, doi: 10.1112/plms/s1-17.1.4.
Ruan, A., J. Li, C. Lee, X. Qiu, and S. Pan, 2012, Passive seismic experiment and ScS wave splitting in the southwestern subbasin of South China Sea: Chinese Science Bulletin, **57**, 3381–3390, doi: 10.1007/s11434-012-5132-0.
Scholte, J. G., 1947, The range of existence of Rayleigh and Stoneley waves: Geophysical Journal International, **5**, 120–126, doi: 10.1111/j.1365-246X.1947.tb00347.x.
Sens-Schönfelder, C., 2008, Synchronizing seismic networks with ambient noise: Geophysical Journal International, **174**, 966–970, doi: 10.1111/j.1365-246X.2008.03842.x.
Shtivelman, V., 2003, Using surface waves for studying the shallow subsurface: Bolletino di Geofisica Teorerica ed Applicata, **44**, 223–236.
Shtivelman, V., 2004, Estimating seismic velocities below the sea-bed using surface waves: Near Surface Geophysics, **2**, 241–247, doi: 10.3997/1873-0604.2004021.
Socco, V. L., D. Boiero, M. Maraschini, M. Vanneste, C. Madshus, H. Westerdahl, K. Duffaut, and E. Skomedal, 2011, On the use of the Norwegian

Geotechnical Institute's prototype seabed-coupled shear wave vibrator for shallow soil characterization — II. Joint inversion of multimodal Love and Scholte surface waves: Geophysical Journal International, **185**, 237–252, doi: 10.1111/j.1365-246X.2011.04961.x.

Stoneley, R., 1924, Elastic waves at the surface of separation of two solids: Proceedings of the Royal Society of London, Series A, **106**, 416–428, doi: 10.1098/rspa.1924.0079.

Vanneste, M., C. Madshus, V. L. Socco, M. Maraschini, P. M. Sparrevik, H. Westerdahl, K. Duffaut, E. Skomedal, and T. I. Bjørnarå, 2011, On the use of the Norwegian Geotechnical Institute's prototype seabed-coupled shear wave vibrator for shallow soil characterization — I. Acquisition and processing of multimodal surface waves: Geophysical Journal International, **185**, 221–236, doi: 10.1111/j.1365-246X.2011.04960.x.

Wald, L. A., and J. Mori, 2000, Evaluation of methods for estimating linear site-response amplifications in the Los Angeles region: Bulletin of the Seismological Society of America, **90**, S32–S42, doi: 10.1785/0119970170.

Xia, J., R. D. Miller, C. B. Park, and G. Tian, 2003, Inversion of high frequency surface waves with fundamental and higher modes: Journal of Applied Geophysics, **52**, 45–57, doi: 10.1016/S0926-9851(02)00239-2.

Xia, J., Y. Xu, and R. D. Miller, 2007, Generating an image of dispersive energy by frequency decomposition and slant stacking: Pure and Applied Geophysics, **164**, 941–956, doi: 10.1007/s00024-007-0204-9.

Xia, Y. J., S. D. Ni, X. F. Zeng, J. Xie, B. S. Wang, and S. Y. Yuan, 2015, Synchronizing intercontinental seismic networks using the 26s persistent localized microseismic source: Bulletin of Seismological Society of America, **105**, 2101–2108, doi: 10.1785/0120140252.

Xu, Y., T. Hao, M. Dai, B. Zhao, J. Li, G. Tu, and Y. Zhao, 2007, Integrated geophysics research on distribution of residual basins of Bohai Sea (in Chinese): Chinese Journal of Geophysics, **50**, 868–881, doi: 10.1002/cjg2.1553.

Xu, Y., T. Hao, S. Huang, Z. Li, C. Lü, B. Zhao, and W. Hu, 2011, Crustal and mantle structure of the Bohai Bay area based on the gravity and magnetic data (in Chinese): Chinese Journal of Geophysics, **54**, 1169–1177, doi: 10.1002/cjg2.1693.

Zhang, L., M. Zhao, J. Wang, E. He, W. Ao, X. Qiu, H. Xu, X. Wei, and J. Zhang, 2013, Correction of OBS position and recent advance of 3D seismic exploration in the central sub-basin of South China Sea (in Chinese): Earth Science — Journal of China University of Geosciences, **38**, 33–42, doi: 10.3799/dqkx.2013.004.

Zhao, M., X. Qiu, S. Xia, P. Wang, K. Xia, and H. Xu, 2008, Identification and analysis of shear waves recorded by three-component OBSs in northeastern South China Sea: Progress in Natural Science, **18**, 181–188, doi: 10.1016/j.pnsc.2007.06.005.

Zhao, M., X. Qiu, S. Xia, H. Xu, P. Wang, T. Wang, C. Lee, and K. Xia, 2010, Seismic structure in the northeastern South China Sea: S-wave velocity and V_P/V_S ratios derived from three-component OBS data: Tectonophysics, **480**, 183–197, doi: 10.1016/j.tecto.2009.10.004.